



Polar bonds induced strong Pd-support electronic interaction drives remarkably enhanced oxygen reduction activity and stability

Qiaoling Li^{a,b}, Xuewei Wang^a, Zhi Xie^a, Xingkai Peng^a, Lingli Guo^a, Xiaofei Yu^a, Xiaojing Yang^a, Zunming Lu^a, Xinghua Zhang^a, Lanlan Li^{a,*}

^a School of Materials Science and Engineering, Hebei University of Technology, Tianjin 300130, China

^b School of Materials Science and Engineering, Shandong University of Technology, Zibo 255000, China

ARTICLE INFO

Keywords:

Strong metal-support interaction (SMSI)
Electron transfer
Oxygen reduction reaction
Porous boron nitride (p-BN)
Polar bond

ABSTRACT

The strong metal-support interaction (SMSI) effect is attractive for improving the activity and durability of metal catalyst. Here, we uncovered that the strong polar bond in support can significantly boost the electrocatalytic oxygen reduction activity and durability of Pd nanoparticles (NPs). The mass-specific activity and surface-specific activity of optimized Pd/p-BNO at 0.90 V (vs.RHE) is almost 1.9 and 2.2 times higher than that of commercial Pt/C catalyst, respectively. By means of a joint experimental and computational study, the enhanced activity of Pd/p-BNO stems from the electron directly transfer through the strong polar O—B bonds from support to Pd NPs leading to the electron-rich Pd surface. Moreover, the strong bonding effect of the caused by polarity bond effectively improves the stability of Pd/p-BNO. This progress demonstrates the vital role of polar chemical bonds in support on inducing SMSI effect, which might open up new opportunities in designing superior heterogeneous catalysts.

1. Introduction

Palladium (Pd), larger reservation (2–3 times), similar electronic structures and chemical properties compared to platinum (Pt), is usually regarded as a potential catalyst for a large number of important chemical reactions [1,2]. Taking oxygen reduction reaction (ORR) as an example, however, the electrochemical performance of Pd is still barely equivalent to that of Pt catalyst because [3–5]: (I) compared to Pt, Pd surface tends to be oxidized at less positive potentials due to its higher d-band center; (II) Pd-based catalyst has a larger electrochemical solubility than Pt-based catalyst under harsh operation conditions of fuel cells. Thus, the insufficient catalytic stability and activity of Pd-based catalysts can lead to an unacceptable drop in ORR performance under long-term fuel cell conditions.

Tremendous efforts have been devoted to tailoring the electronic structure of Pd to enhance its catalytic activity, such as alloying Pd with another metal to form an alloy, forming a core-shell structure to achieve strain effect and changing its support to form strong metal-support interaction (SMSI) [6–11]. The SMSI strategy appears most promising because it significantly reduced the amount of metal especially precious metals and further improved both the ORR activity and durability.

Carbon materials have been conventionally used as popular supports for metal catalysts due to its good electrical conductivity and large specific surface area. The sp^2 carbon materials have abundant freely movable π electrons in-plane, however, it is too inert to have a directed electron transfer with metal out of plane [12,13]. This makes a weak interaction between metal and carbon supports, so it is very difficult to tailor the electronic structure of Pd. Construction of the charge transfer process between metal catalysts and substrates therefore provides the key for the formation of SMSIs.

It has been revealed that the carbon π electrons can be activated by doping with other heteroatoms (e.g. N, B, S, etc.) [14–19]. Among them, the N with larger electronegativity can readily interact with the carbon and lone-pair electrons from N dopants donate into carbon structure, which results in tunable chemical properties and facilitated charge transfer. By B doping, the π electrons become quite active due to the low electronegativity and electron-deficient property of B. Breaking the electroneutrality of C=C chemical bond in support may be the key to optimize the interaction at the metal/support interface [20–23], in this context, introducing polar bonds to the support would tailor the electronic structure of metal catalyst via electron transfer. This is because, with the introduction of polar bonds, the redistribution of electron with

* Corresponding author.

E-mail address: liabc@hebut.edu.cn (L. Li).

<https://doi.org/10.1016/j.apcatb.2021.121020>

Received 19 October 2021; Received in revised form 29 November 2021; Accepted 16 December 2021

Available online 18 December 2021

0926-3373/© 2021 Published by Elsevier B.V.

local depletion and accumulation lead to more anchoring sites and facilitates directional charge transfer between metal and support. For example, the B-doped graphene sheets (GS) can strongly anchor Pd on the bridge site of B—C bonds other than that on C—C bonds, and the polar B—C bond boosts the electron coupling between Pd NPs and support [21]. The doping of carbon nanotube with N (NCNTs) has also been reported to enable an electronic modification of the immobilized Pd by the electron interaction between Pd and support [23]. Hence, the forming of polar C—X (X = N, B, S, etc.) bond in carbon materials is of vital importance for promoting electron transfer between support and metal.

Simultaneously, recent studies have shown that hexagonal boron nitride (h-BN) with polar B—N bonds is a promising metal catalyst support because its excellent thermal conductivity, oxidation resistance, and chemical stability make it to withstand electrochemical corrosion [24–29]. Additionally, Sun et al. reported that h-BN not only serves as a durable platform in the h-BN/Pd heterostructured electrocatalysts, but also endows catalysts surfaces with superhydrophobic property, promoting the diffusion kinetics of O₂ for ORR [30]. Importantly, our previous work has reported that polar B—N bonds enable the electron donation-back donation process between support and Pt catalyst, which strengthen the SMSI effect between Pt and BN support and regulate the electronic structure and activity of Pt catalyst [31]. Challenges, however, still exist with using BN: when the electronegativity of metal is less than Pt (such as Pd), the electron donation-back donation effect between metal and B—N bond is weak and could rarely realize electrons directional transfer. Hence, BN support may improve the durability of Pd catalyst but cannot tune its electronic structure fundamentally. To realize directional electrons transfer, it is necessary to introduce polar covalent bonds with larger polarity.

Herein, a controllable route was proposed to introduce O—B bonds to the porous boron nitride (p-BN) in different concentrations to obtain oxygen-doped porous boron nitride (p-BNO) supports via a facile two-step approach. Compared to C support with covalent C—C bond and h-BN support with polar covalent N—B bond (electronegativity: B = 2.04, N = 3.04), the p-BNO with strong polar O—B bond (electronegativity: B = 2.04, O = 3.44) supported Pd NPs (~4.4 nm) exhibits excellent ORR performance. As expected, the O—B sites can be as both the active site to anchor Pd NPs and the plentiful surface donors to activate the Pd catalyst, facilitating the ORR process. Benefit from directional electrons transfer from O—B to the Pd NPs, the newly developed Pd/p-BNO catalyst exhibits ORR catalytic activity outperforms that of commercial Pd/C (Com. Pt/C) in both alkaline and acidic media. Moreover, this work inspires a new consideration in the field for how to induce the SMSI effect to boost the ORR electrocatalysis.

2. Experimental and computational methods

2.1. Preparation of p-BNO materials

The p-BNO was synthesized by precursor preparation and subsequent thermal treatment methods as we used in our previous work [31]. To introduce O—B contaminations, boric acid (H₃BO₃) which contains proper O—B bonds was used as the source of boron in the synthesis of p-BNO. First, H₃BO₃ and melamine (C₃N₆H₆) with molar ratio of 3:1 was dissolved in distilled water and kept at 90 °C for 3 h. Next, the solution was cooled at different temperature to obtain white precursor i.e. M-2B. Here, to obtain precursors with different oxygen content, we regulate the precipitation rate of C₃N₆H₆·2H₃BO₃ (M-2B) precursor by controlling precipitation temperature to realize the different pyrolysis kinetics of M-2B [32]. Then the obtained precursors were dried at 60 °C for 12 h and finally heated at 1100 °C for 4 h under flowing N₂ atmosphere to obtain p-BNO samples with different O—B concentration.

2.2. Preparation of Pd/p-BNO catalysts

The Pd particles were loaded onto p-BNO by an impregnation reduction process. Firstly, 30.0 mg BN supports (as-prepared p-BNO samples or Com. h-BN) were dispersed ultrasonically into 20.0 mL distilled water for 0.5 h. Next, 1.56 mL Na₂PdCl₄ aqueous solution (0.02 M) was added into the above formed solution. After stirring for 6 h, the resulting mixture was reduced by NaBH₄ (24.0 mg) and then stirred for 20 min. The obtained precipitates were separated by centrifugation, washed with distilled water and then vacuum dried for 48 h to obtain Pd/p-BNO and Pd/h-BN catalysts.

2.3. Structural characterizations

The crystal structure and chemical composition of as-prepared supports and catalysts were performed using X-ray diffractometer (XRD) (Cu K α radiation, Bruker D8 Discover), Fourier-transform infrared (FTIR) spectrometer (Vetext 80 V, Bruker Corp., USA), Raman spectroscopy (CRM200 Raman system, with a 532-nm laser, Witec Corp., USA) and X-ray photoelectron spectroscopy (XPS) (Vetext 80 V, Bruker Corp., USA) spectrometer under vacuum. The contents of oxygen were analyzed by a nitrogen/oxygen determinator (LECO, TC500). The Brunauer-Emmett-Teller (BET) specific surface area was measured on a N₂ adsorption-desorption isotherms measured at 77 K using a novel 4000e (Quantachrome) analyzer. The Pd contents of samples were determined by an inductively coupled plasma mass spectrometry (ICP-MS, TELEDYNE-Leeman Labs, USA). The morphologies of the samples were characterized by scanning electron microscopy (SEM) (S-4800, Hitachi Ltd., Japan), transmission electron microscopy (TEM), and high-resolution transmission electron microscopy (HRTEM) with a 200 kV accelerating voltage (FEI Tecnai F20).

2.4. Electrochemical measurements

Catalyst ink was prepared with an ultrasonic mixture of 2 mg catalyst, 800 μ L isopropanol, 30 μ L 5 wt% Nafion solution and 200 μ L deionized water for 30 min. Certain microliters of the catalyst ink were dropped onto the glassy carbon substrate of rotating disk electrode (RDE, 3 mm in diameter, Pine Instruments), and then dried at room temperature. The loaded mass of Pd on RDE was normalized as ~15 and ~20 μ g cm⁻² for Pd/BN(or BNO) and Com. Pd/C (10 wt%) catalyst, respectively. Pt loading of Com. Pt/C (20 wt%) was fixed at ~20 μ g cm⁻² unless otherwise specified.

All the electrocatalytic experiments were carried out using an electrochemical workstation (CHI760E, Shanghai Chenhua Instrument Co., Ltd., China), which connected with a rotating ring-disk electrode rotator (RRDE-3A, ALS, Japan). All the measurements were executed with a standard three-electrode system at room temperature. The work electrode is the catalyst coated RDE. A graphite rod and a saturated Ag/AgCl electrode were used as the counter and reference electrode respectively. All potentials in this paper were converted to values referring to the reversible hydrogen electrode (RHE).

Cyclic voltammetry (CV) tests were performed in the potential range of 0.05–1.20 V in N₂-saturated 0.1 M HClO₄ solution with a scan rate of 50 mV s⁻¹. Linear sweep voltammetry (LSV) measurements were carried out in an O₂-saturated electrolyte solution through the RDE method at 10 mV s⁻¹ and 1600 rpm. The H₂O₂ yield was measured using a glassy carbon ring-disk electrode with a Pt ring (UA011 Pt-GC, RRDE). The stability of the catalysts was assessed by scanning the working electrode in an O₂-saturated electrolyte solution with the potential range of 0.60–1.10 V at 100 mV s⁻¹ for 5000 durability cycles. Electrochemical impedance spectroscopy (EIS) was measured from 100 kHz~0.01 Hz at 0.85 V for ORR.

2.5. Density functional theory (DFT) calculations

The spin-polarized DFT calculations were performed by the Vienna ab initio simulation package (VASP) [33]. The Projector-augmented-wave (PAW) potentials [34] with the energy cutoff of 450 eV were used to account the electron-ion interactions. The Generalized Gradient Approximation (GGA) with Perdew-Burke-Ernzerhof (PBE) was used to analyze electron exchange-correlation functional in the calculations [35]. Atomic structures were fully relaxed until the force on each atom was $0.01 \text{ eV } \text{\AA}^{-1}$, and the energy convergence threshold was set to 10^{-6} eV . In the geometrical optimization, $5 \times 5 \times 1$ k-meshes connecting specific points of the Brillouin zone were employed to ensure that the total energy converged to $\sim 1 \text{ meV}$. Furthermore, $9 \times 9 \times 1$ k-meshes connecting specific points of Brillouin zone were adopted for calculations of electronic density of states (DOSs). The geometric and electronic structures of Pd catalyst loaded on each support were calculated to understand the effects of the supports.

3. Results and discussion

3.1. Characterization of p-BNO support

Firstly, the detailed O mass contents of as-prepared samples were determined by nitrogen/oxygen determinator measurement and the mass percentage of O in two p-BNO samples are 26.70 wt% (denoted as p-BNO-1, corresponding to precursor M-2B precipitated at 16°C) and 36.70 wt% (denoted as p-BNO-2, corresponding to precursor M-2B precipitated at 30°C), respectively. For comparison, the mass percentage of O in commercial h-BN (Com. h-BN) was also determined to be

0.76 wt%.

Next, all the XRD patterns for the synthesized p-BNO samples and Com. h-BN can be indexed to the hexagonal-type BN (JCPDS No. 45-895) in which the peaks at $\sim 26.7^\circ$ and $\sim 43.1^\circ$ are indexed to characteristic (002) and (100) planes (Fig. S1a). As compared to Com. h-BN the XRD peaks of the synthesized p-BNO samples are broader and show lower crystallinity. Besides, the 2 θ peak of the (002) plane obviously shifts from 26.8° (Com. h-BN) to 25.8° for p-BNO-1 and to 25.4° for p-BNO-2 respectively, and correspondingly TEM shows the interplanar distance increased distinctly (Fig. S1b). In addition, Raman spectrum was investigated to further verify the crystalline ordering of the p-BNO samples (Fig. 1a). The Raman peaks of p-BNO-1 and p-BNO-2 locate at 1374.0 and 1375.9 cm^{-1} respectively, which are close to that of highly crystallized h-BN (1365.5 cm^{-1}). The slightly shift toward a higher frequency may be attributed to a gradually increase of oxygen defects, which lead to the expansion of BN layers and an increasingly weaker BN interlayer interaction, and then contributes to the improvement of electronic band structures [36,37].

Then, the microscopic morphology and structural of the synthesized p-BNO samples are displayed in Fig. S2a,b. Observation from SEM images shown in Fig. S2 indicate that the synthesized p-BNO samples present fiber-like morphology with relatively uniform size and the average diameters of the fibers are $\sim 0.77 \mu\text{m}$ for p-BNO-1 and $\sim 2.33 \mu\text{m}$ for p-BNO-2 respectively. Moreover, the N_2 adsorption-desorption isotherms (type IV with hysteresis) of the p-BNO-2 samples indicate the existence of both micropores (~ 1.3 , $\sim 1.6 \text{ nm}$) and mesopores (~ 2.4 , ~ 5.0 and $\sim 8.0 \text{ nm}$) (Fig. S3). The specific surface areas of p-BNO-1 and p-BNO-2 are 1109.54 and $753.84 \text{ m}^2 \text{ g}^{-1}$, respectively. Compared to p-BNO-1 the surface area of p-BNO-2 samples is decreased because of a more serious O-B series related glassy surface [38].

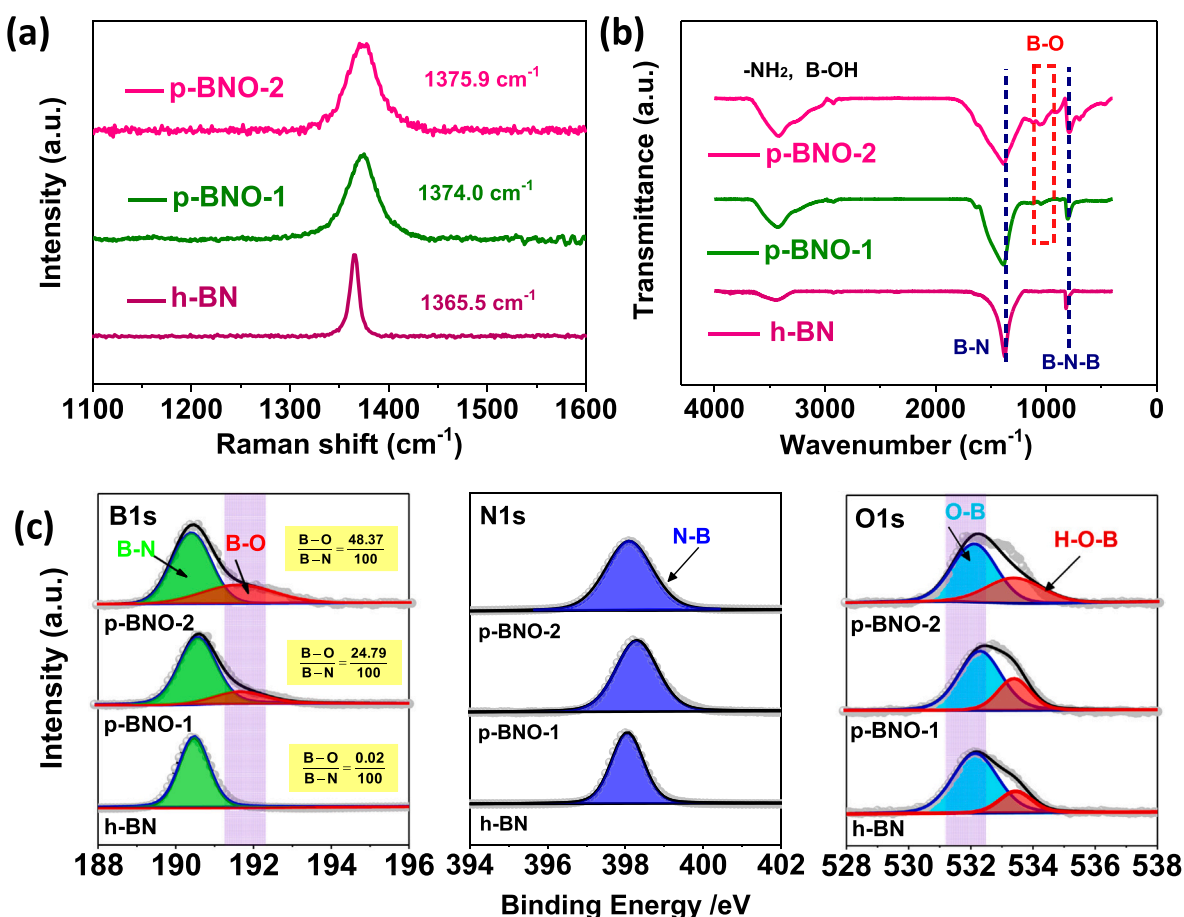


Fig. 1. (a) Raman, (b) FTIR, and (c) XPS patterns of h-BN, p-BNO-1, and p-BNO-2 samples, respectively.

Finally, the FTIR spectras and XPS measurements were performed to confirm the successful introduction of O—B bond (Fig. 1b). In FTIR spectras, two characteristic peaks at ~ 810 and ~ 1376 cm^{-1} corresponding to B—N—B (out-of-plane bending vibrations) and B—N (in-plane stretching vibrations) bonds, respectively [39,40]. Importantly, there is a band in the range of $904\text{--}1108$ cm^{-1} corresponding to the O—B bending vibration [40,41]. This is in contrast to the h-BN which does not show active O—B vibrations at the corresponding locations. Moreover, compared to h-BN, a red-shift in the adsorption edge from 3272 cm^{-1} for h-BN to 2992 cm^{-1} for p-BNO-1 and 2982 cm^{-1} for p-BNO-2 respectively, reveals an increase of the B—OH vibrations in p-BNO samples. These results reveal that the O—B bonds were successfully introduced in p-BNO samples. The presence of O—B bond in p-BNO samples was further confirmed by XPS spectroscopy (Fig. 1c). The B 1s and N 1s XPS spectrums of both p-BNO samples primarily reflect the chemical states of typical B—N (190.40 eV) and N—B (398.00 eV) peaks for intrinsic BN [36, 42]. The sub-peak located at 191.61 eV in the B1s spectrum corresponds to B—O bonding [37,42], indicating that O—B bonds were successfully introduced. Moreover, it is worth noting that the ratio of B—O to B—N increased from $0.02:100$ for h-BN to $24.79:100$ for p-BNO-1 and $48.37:100$ for p-BNO-2 respectively. The O 1s spectrum of all samples was deconvoluted into two bands of O—B and H—O—B bonding structures at 532.06 eV and 533.50 eV, respectively. All these results confirmed that the oxygen element in the p-BNO samples is mainly in the form of

O—B bond. Therefore, the p-BNO is oxygen-doped porous boron nitride with a high O—B bond content.

3.2. Characterization of Pd/p-BNO catalysts

XRD patterns shown in Fig. 2a exhibit the characteristic diffraction peaks of the as-prepared Pd/p-BNO-1, Pd/p-BNO-2, Pd/h-BN, and commercial Pd/C (Com. Pd/C, 10 wt%) catalysts, confirming the successful loading of Pd species on the supports. For Pd/p-BNO-1 and Pd/p-BNO-2 catalysts, the Pd(111) diffraction peak slightly shifted from 40.1° to 39.6° (Pd/p-BNO-1) and 39.1° (Pd/p-BNO-2) respectively, suggesting a Pd-Pd lattice enlargement when loaded on p-BNO supports. Furthermore, the Pd diffraction peaks for Pd/p-BNO-1,2 samples are found to be distinctly broadened, indicating that Pd NPs dispersed with a smaller size on the p-BNO supports. TEM images prove that Pd NPs are uniformly anchored on h-BN (Fig. S4a,b), p-BNO-1 (Fig. S4c,d) and p-BNO-2 (Fig. 2b–d) supports and have an average particle size of 6.8 ± 0.5 nm (on h-BN), 4.1 ± 0.5 nm (on p-BNO-1) and 4.4 ± 0.5 nm (on p-BNO-2) respectively. The contents of Pd were determined to be ~ 9.0 wt% in Pd/h-BN, ~ 8.7 wt% in Pd/p-BNO-1 and ~ 8.6 wt% in Pd/p-BNO-2 respectively by ICP-MS analysis. The EDX mapping images in Fig. 2c present a uniform distribution of N, O, B, and Pd elements in the Pd/p-BNO-2 sample. It is noteworthy that there is a lattice expansion of Pd when loaded on p-BNO. In the case of Pd/p-BNO-1 (Fig. S4d), the interplanar

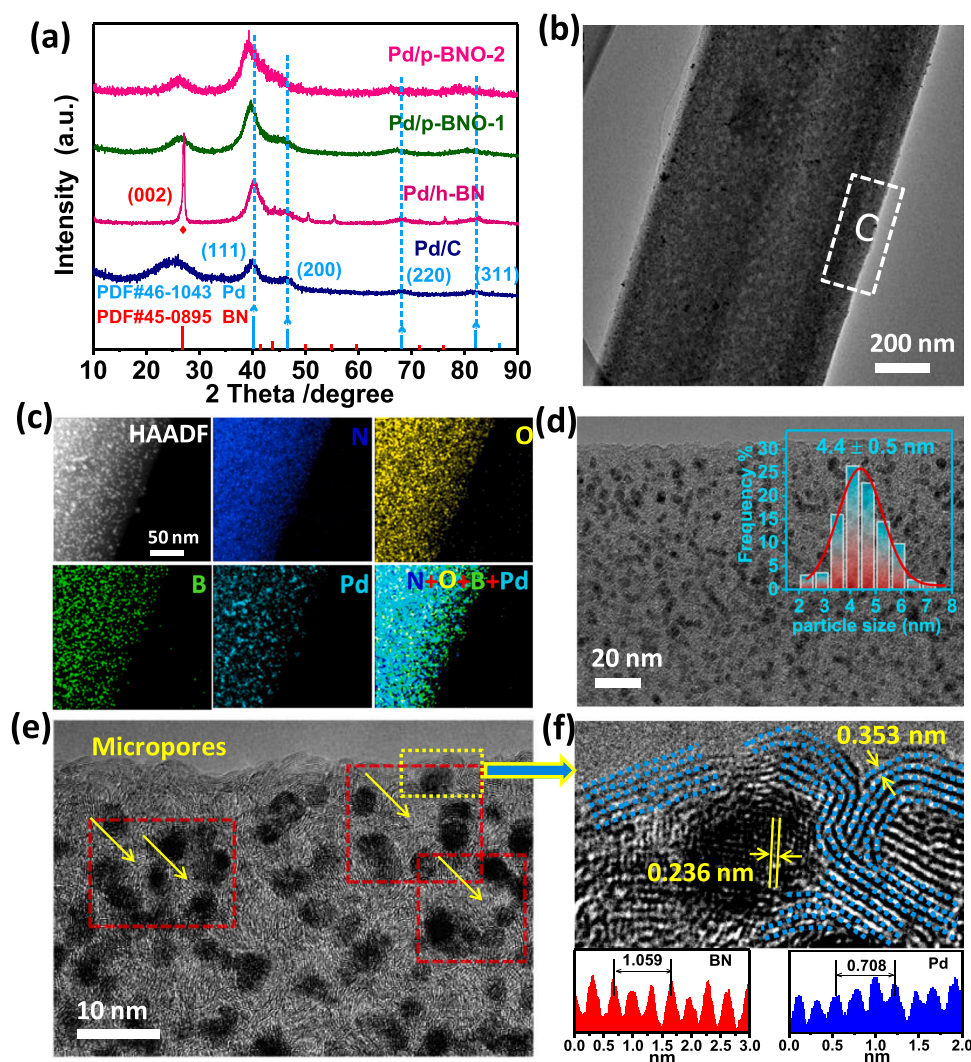


Fig. 2. (a) XRD of Pd/h-BN, Pd/p-BNO-1,2, and Pd/C samples. (b) TEM, (c) HAADF-STEM images with the corresponding EDS elemental mapping, and (d) TEM of the Pd/p-BNO-2 sample with the size distribution of Pd particles. (e) TEM and (f) HRTEM and the contrast intensity profiles of Pd/p-BNO-2.

spacing of 0.228 nm observed in HRTEM, which correspond to Pd (111) plane, is larger than that of Pd/h-BN (0.225 nm, see Fig. S4b). With the increases of O-B impurity, the interplanar spacing of Pd further increased to 0.236 nm for Pd/p-BNO-2 (Fig. 2e,f), resulted in a lattice expansion degree of 4.8% compared with that of the Pd/h-BN. These results indicate the existence of tensile lattice strain for Pd NPs due to the strong interaction with O-B bond. The strain effect is proven to contribute to the optimization of the electrocatalytic activity and durability of noble metal NPs. It has been reported that the tensile strain is beneficial to the activation of low-coordinated surface atoms and thus enabling optimal oxygen binding energies as well as improving ORR catalytic performances [43,44]. Moreover, after Pd loading, the micropores can also be identified in the TEM image (Fig. 2e). Concomitantly, the Pd/p-BNO-2 sample still possesses a high BET surface area ($390.57 \text{ m}^2 \text{ g}^{-1}$) and keeps a similar characteristic pore sizes with p-BNO-2 (Fig. S3). It is important to note that, the existence of micropores and mesopores could provide sufficient space for the mass transport of reactant and the diffusion of O_2 .

The surface composition and chemical states of Pd/p-BNO-2 were further detected by high-resolution XPS spectra, as shown in Fig. 3. The XPS survey spectrum clearly confirmed the presence of B, N, O and Pd of Pd/p-BNO-2 (Fig. S5a). High-resolution XPS spectra of B 1s, N 1s, O 1s, and Pd 3d (Fig. 3a-d) were obtained to study the changes of surface states after Pd loading. After Pd loading, 191.61 eV peak of B-O bond was significantly shifted to 191.16 eV in B 1s spectra concomitant with O-B bond shift from 532.06 eV to 532.52 eV in O 1s spectra, revealing that there is a strong electronic coupling between O-B bonds and Pd (O-B...Pd) [45]. Moreover, as shown in O 1s spectra (Fig. 3c), the H-O-B almost disappears after Pd loading, confirming the roles of the O-B moieties as pivotal sites for O-B...Pd binding. In contrast, as shown

in Fig. S5b, there are no obvious changes on the three resolution peaks in C 1s spectrum, suggesting that the interaction between the C atom and Pd is negligible, if any. Hence the introduction of O-B in p-BN strengthened the interaction between Pd NPs and the support in the Pd/p-BNO system, serving as a potential barrier to inhibit the electrochemical dissolution of Pd under the harsh operating conditions. The high-resolution Pd 3d XPS spectra are shown in Fig. 3d. The Pd/h-BN sample and Com. Pd/C was also measured for comparison. On the one hand, the surface atomic proportion of Pd^0 and Pd^{2+} were estimated based on the XPS peak areas and the ionization cross section of the energy level of Pd 3d [45]. The results show that Pd^0 percentage contents in Pd/C, Pd/h-BN, and Pd/p-BNO-2 is approximately 44.21%, 52.55% and 66.97%, respectively, revealing that the majority of surface Pd in Pd/p-BNO-2 is in metallic state. On the other hand, a careful inspection of the Pd 3d spectra shows that the binding energy in Pd/h-BN (335.66 eV) negatively shifts $\sim 0.13 \text{ eV}$ and that in p-BNO-2 (335.52 eV) negatively shifts $\sim 0.27 \text{ eV}$ relative to those in Com. Pd/C (335.79 eV). Therefore, these results indicate that Pd in the Pd/p-BNO-2 structure is enriched with electrons owing to the electron transferring from the O-B to Pd. This may be due to the larger polarity of O-B bond and the detailed evidence will be given later by DFT calculations.

3.3. Electrocatalytic ORR performance of Pd/p-BNO catalysts

To evaluate the effect of polar bonds in the support on the catalytic property of metal, we assessed the catalytic properties of three kinds of Pd-based catalysts with different supports: Com. Pd/C catalyst (10 wt%) in which support mainly contains C=C covalent bond, Pd/h-BN catalyst (9.0 wt%) in which support composed of B-N polar covalent bond, and Pd/p-BNO catalyst (Pd/p-BNO-1, 8.7 wt% and Pd/p-BNO-2, 8.6 wt%) in

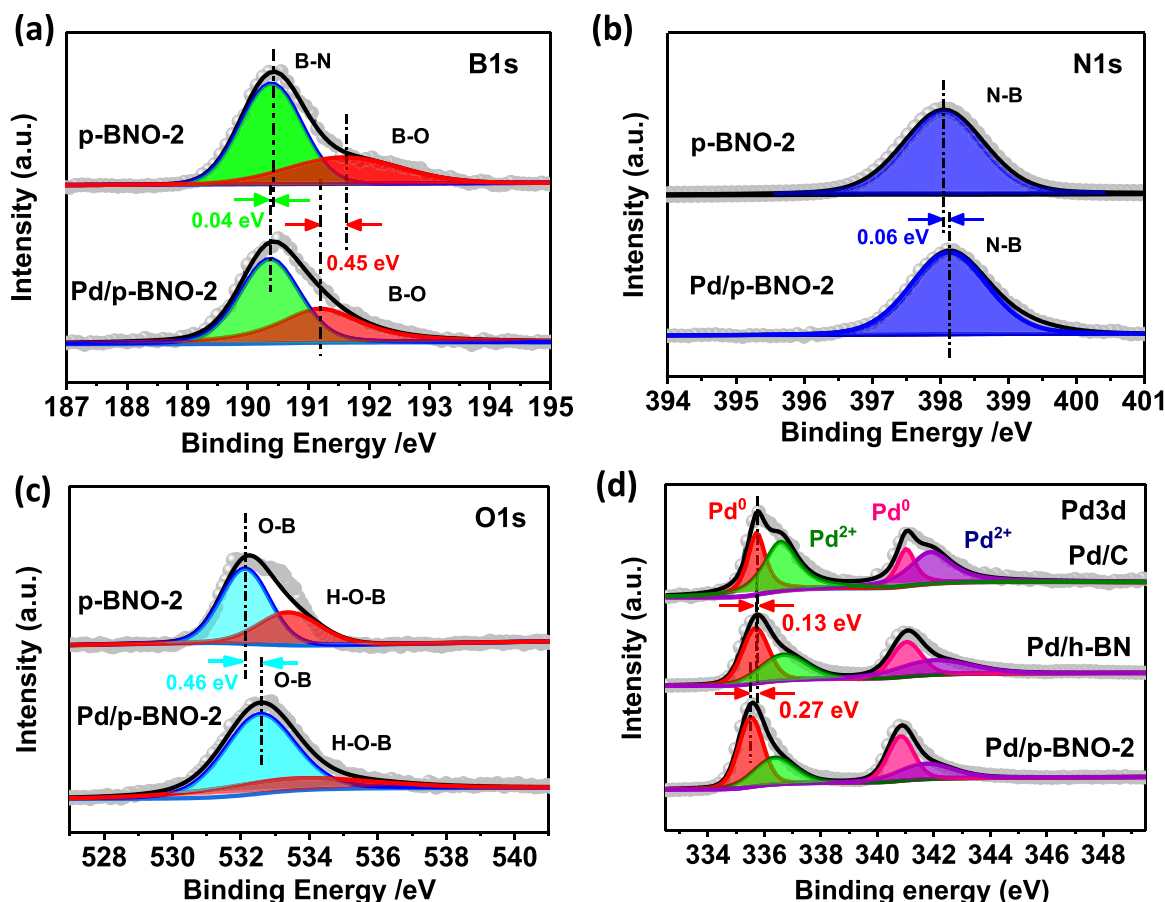


Fig. 3. The XPS patterns of (a) B 1s, (b) N 1s, and (c) O 1s for p-BNO-2 and Pd/p-BNO-2, and (d) Pd 3d for Pd/p-BNO-2, Pd/h-BN, and Com. Pd/C.

which support contains both O—B and B—N polar covalent bond (Fig. 4).

Firstly, the ECSA were determined by recording the CO stripping voltammograms (Fig. S6) and the results are compared in Fig. 4a. The ECSA of the Pd/p-BNO-2 is calculated to be $60.66 \text{ m}^2 \text{ g}^{-1}_{\text{Pd}}$, which is higher than those of Pd/p-BNO-1 ($56.28 \text{ m}^2 \text{ g}^{-1}_{\text{Pd}}$), Pd/h-BN ($47.39 \text{ m}^2 \text{ g}^{-1}_{\text{Pd}}$) and Com. Pd/C ($34.50 \text{ m}^2 \text{ g}^{-1}_{\text{Pd}}$), and closes to that of Com. Pt/C ($67.27 \text{ m}^2 \text{ g}^{-1}_{\text{Pt}}$). These results coincide with the ECSA estimated from integrated H_{upd} charge of Com. Pt/C and Ox_{red} charge of Pd-based electrodes (Figs. S7, 4a). The bigger ECSA of Pd/p-BNO catalyst indicates that more active sites and additional specific surface area will appear when Pd loaded on p-BNO support which contains more polar bonds.

Secondly, the ORR polarization curves are shown in Fig. 4b. Compared with Com. Pd/C, all Pd/BN electrodes (Pd/h-BN and Pd/p-BNO-1,2) exhibit much higher activity in the catalysis of ORR, indicating that polar bond in support can dramatically boost the activity of Pd and thus reducing the electrochemical polarization. The half-wave potentials of ORR on Pd/BN electrodes positively shift in the order Pd/h-BN < Pd/p-BNO-1 < Pd/p-BNO-2, revealing that the polar bond with larger polarity in support is favorable to ORR process. Specifically, Pd/p-BNO-2 electrode achieves the most positive half-wave potential ($E_{1/2}$) of $\sim 0.89 \text{ V}$, which is even 30 mV more positive than that on Com. Pt/C electrode ($\sim 0.86 \text{ V}$). Moreover, the MA of p-BNO-2 is $0.253 \text{ A mg}^{-1}_{\text{Pd}}$, which is nearly 2.0 and 4.1 times higher than that of the Com. Pt/C ($0.123 \text{ A mg}^{-1}_{\text{Pt}}$) and Pd/C ($0.061 \text{ A mg}^{-1}_{\text{Pt}}$) catalysts, respectively (Fig. 4c). Noteworthy, the resulting ratio of MA (Pd/p-BNO-2): MA (Com. Pd/C) is much higher than that of SA (Pd/p-BNO-2): SA (Com. Pd/C). The improvement of the mass activity of Pd/p-BNO-2 is due both to the increase of specific electrochemical active surface area and to the improvement of the intrinsic activity of Pd with the modified electronic structure (Fig. S8).

Thirdly, we probe into the kinetics of ORR over these Pd-based electrodes. EIS measurements were performed to explore the charge-

transfer properties involved in the electrode/electrolyte interface during the ORR process (Fig. 4d). Although h-BN has poor conductivity, oxygen doping has been proven to enhance electrical conductivity of BN materials and its bandgap can be narrowed to 1.7 eV [36]. The diameter of the partial semicircle in the high-frequency region for Pd/p-BNO-1 and Pd/p-BNO-2 electrodes are much lower than that in Com. Pd/C and even lower than that in Com. Pt/C, suggesting the introduction of polar bonds contributes to promoting interfacial charge transfer process. Moreover, the number of electron transfer (n) and the yield of H_2O_2 were measured using a rotating ring-disk electrode (RRDE). As presented in Fig. 4e, the n values of Pd/p-BNO-1 (3.92–3.98) and Pd/p-BNO-2 (3.95–3.99) are higher than that of both Com. Pd/C and Com. Pt/C and close to 4. Accordingly, the H_2O_2 yield for Pd/p-BNO-2 is only 0.63–2.17%, significantly lower than that for Com. Pd/C and even lower for Com. Pt/C (2.07%–6.14%). Additionally, the electron transfer number of Pd/p-BNO-2 was also calculated based on Koutecky-Levich (K-L) plots and the result confirms that the ORR on Pd/p-BNO-2 process via $4e^-$ transfer reaction (Fig. S9). These results manifest that the $4e^-$ selectivity of ORR process on Pd surface increases with the introduction of polar bonds in the supports.

Additionally, the CO-oxidation peak potential was extracted to characterize CO tolerance of the electrodes (Fig. 4f). The CO-oxidation peak potential of Pd/h-BN (0.92 V) has a negative shift of 30 mV with compared to Com. Pd/C (0.95 V), suggesting a better CO tolerance in Pd/h-BN. With the introduction of O—B bond, the CO-oxidation peak potential further negative shift to 0.88 and 0.84 V for Pd/p-BNO-1 and Pd/p-BNO-2 respectively, indicating a further weakening of the CO adsorption energy. This result also confirms the changed electronic structure of Pd by the polar chemical bonds in supports.

The ORR activity was also evaluated in 0.1 M HClO_4 and 0.1 M PBS aqueous solutions, respectively (Fig. S10). In both acidic and neutral electrolytes, the catalytic activity of Pd increases with the introduction of polar bond in support. Especially, in acidic electrolyte, the positively shift of $E_{1/2}$ on the Pd/p-BNO-2 is up to 70 mV compared with Pd/C. In

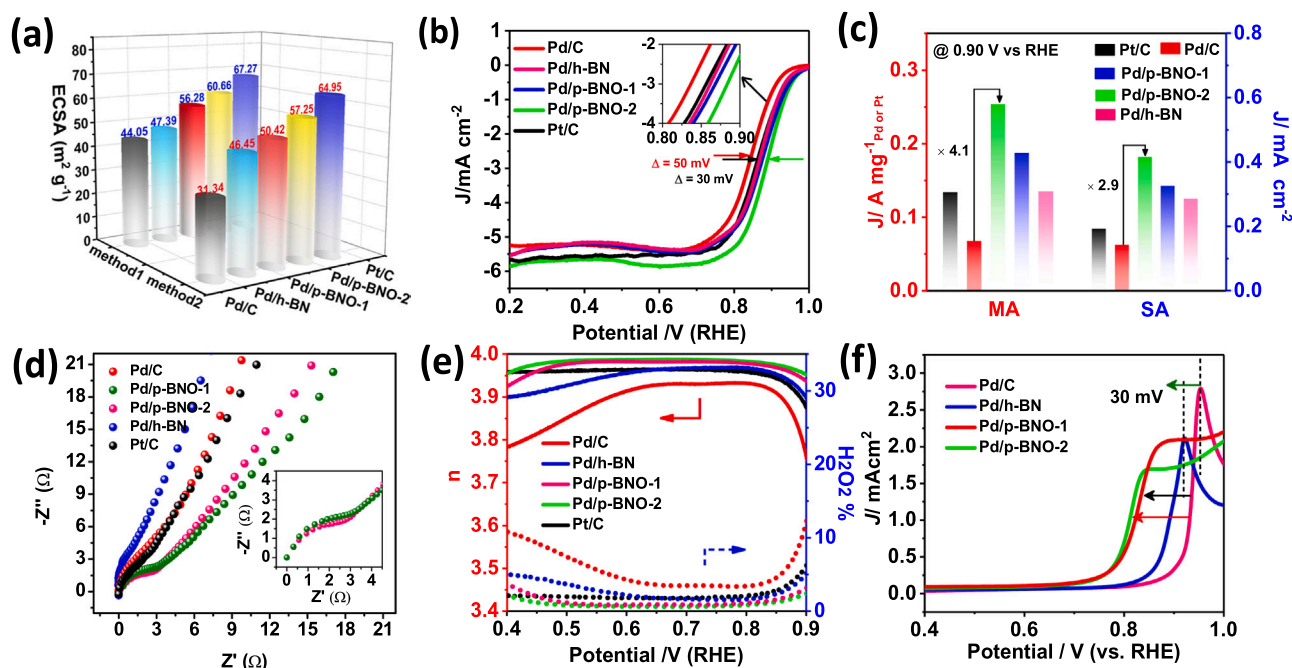


Fig. 4. (a) Normalized ECSAs of Com. Pt/C, Com. Pd/C, Pd/h-BN, Pd/p-BNO-1, and Pd/p-BNO-2 catalysts with different methods (Figs. S6,7). (b) ORR polarization curves of catalysts performed in O_2 -saturated 0.1 M KOH (Scan rate, 10 mV s^{-1} ; rotation rate, 1600 rpm). (c) Comparisons in mass-specific activity (MA) and surface-specific activity (SA) at 0.90 V (vs.RHE). (d) Nyquist plots of Pd/p-BNO-1, Pd/p-BNO-2, Pd/h-BN, Com. Pd/C and Pt/C performed in O_2 -saturated 0.1 M KOH solution at 0.83 V (vs.RHE) (rotation rate, 1600 rpm). The inset shows EIS curves at a high-frequency region. (e) RRDE results for the determination of electron transfer number (n , left) and H_2O_2 yields ($\text{H}_2\text{O}_2\%$, right). (f) The CO-oxidation peaks potential of Com. Pd/C, Pd/h-BN, Pd/p-BNO-1, Pd/p-BNO-2 between 0.40 and 1.00 V (vs.RHE) was extracted from CO stripping voltammograms.

addition, compared with the recently reported supporting Pd catalyst, as-prepared Pd/p-BNO-2 achieves the highest $E_{1/2}$ and MA with a lower Pd loading mass (Table S1).

3.4. The Electrocatalytic durability of Pd/p-BNO catalysts

The electrochemical durability of Pd/p-BNO-2 catalyst for ORR was evaluated by conducting accelerated durability tests (ADTs) in both 0.1 M KOH and 0.1 M HClO₄ (Fig. 5). Both Com. Pd/C and Com. Pt/C catalysts were also tested for comparison. As shown in Fig. 5a–c, after 5000 sweeping cycles in 0.1 M KOH electrolyte, the ORR performance exhibits negligible degradation on the Pd/p-BNO-2 catalyzed electrode, as opposed to 26 mV and 15 mV negative shifts in $E_{1/2}$ of the Com. Pd/C and Com. Pt/C. Simultaneously, the diffusion-limiting current decreased noticeably for Com. Pd/C electrode, suggesting the loss of Pd NPs during the ADT test which originates from the weak interaction between Pd NPs and carbon materials. The MA for Pd/p-BNO-2 showed a tiny loss of Pd activity (6.10%), in sharp contrast to an obvious loss of activity observed for Com. Pd/C (64.22%) and Com. Pt/C (36.68%), indicating that carbon support was corroded while p-BNO is stable enough to withstand the harsh corrosive environment of Fuel cell cathodes. Besides, the ORR decay observed in 0.1 M HClO₄ is larger than that observed in 0.1 M KOH, because acidic electrolyte is a more severe electrochemical condition for both Pd-based and Pt-based catalysts. As shown in Fig. 5d–f, after 5000 cycles, there are 7 mV, 77 mV and 17 mV decline in the $E_{1/2}$ and 15.41%, 72.79%, and 31.34% drop in the MA for Pd/p-BNO-2, Com. Pd/C and Com. Pt/C catalyzed electrode, respectively, indicating the Pd/p-BNO-2 exhibits superb catalytic durability than Com. Pt/C and Com. Pd/C.

The stability of the Pd/p-BNO-2 catalyst under basic ORR conditions was further confirmed by TEM before and after ADT test. The structure of Pd/p-BNO-2 catalyst is well preserved after ADT test and the Pd NPs maintain the uniform dispersion with only a slight change in

nanoparticle diameter from 4.4 ± 0.5 – 5.0 ± 0.5 nm (Fig. S11a,b). However, both Com. Pd/C (Fig. S11c,d) and Com. Pt/C (Fig. S11e,f) showed an evident particle aggregation under the same ADT conditions. Especially, Com. Pd/C catalyst showed the most serious particle conglomeration and most of Pd NPs became two times larger than their initial size, suggesting a weaker interaction between Pd NPs and carbon materials. Here, the enhanced ORR durability of Pd/p-BNO-2 can be understood by the combined influence of the followings: (1) the O–B bonds with larger polarity are more effective than N–B bond and covalent C=C bond for anchoring Pd NPs, (2) the idiographic electronic interaction with polar O–B bonds renders Pd catalyst less oxophilic, and (3) BN materials are stable enough to withstand electrochemical corrosion, as we have previously reported [31].

3.5. Density functional theory calculation

3.5.1. Construction and design of catalyst models

To further clarify the origin of the constructed SMSI between support and Pd NPs for enhanced ORR stability and activity, the density functional theory (DFT) calculations were comprehensively performed (Computational details is shown in the Section S2). More specifically, we constructed the theoretical models of Pd clusters supported on the graphene (characterized with C=C covalent bonds), h-BN (characterized with B–N polar bonds) and O doped h-BN (denoted as h-BNO and characterized with both B–N polar bonds and O–B strong polar bonds), respectively. Basically, the bond dipole moment (μ) of the chemical bond was calculated and used as the indicator of the bond polarity [46]. Here, the dipole moment of O–B was calculated to be 4.52 D for model h-BNO, which is evidently greater than that of N–B for model h-BN ($\mu = 0.95$ D) (Fig. S12). Therefore, the polarity of chemical bonds in support increases in the order: C=C < B–N < O–B.

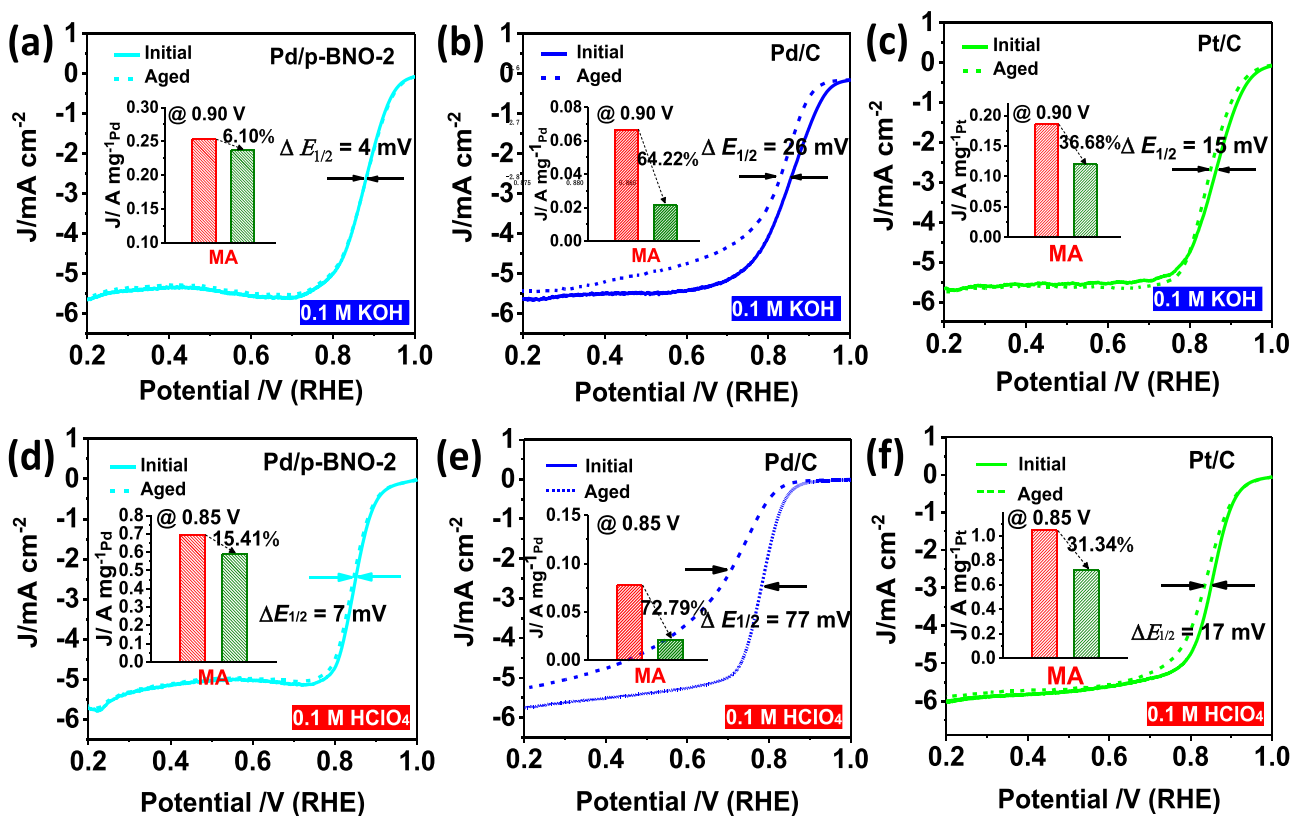


Fig. 5. ORR polarization curves and Mass activities of Pd/p-BNO-2 (a, d), Com. Pd/C (b, e), and Com. Pt/C (c, f) before and after accelerated durability tests (5000 CV cycles) in O₂-saturated 0.1 M KOH and 0.1 M HClO₄ solution.

3.5.2. Tailoring electronic structure of catalysts

In order to probe into the influence of the polar chemical bonds on the electron transfer between Pd and support, the differences in charge density (Fig. S13) and Bader charge (Table S2) were firstly calculated, schematically, in Fig. 6a. For Pd₅/Graphene, the charge density is partially depleted around Pd atoms, while accumulated around C atoms, and bader charge analyses indicate an electron transfer of 0.275 |e| from the Pd cluster to support. With the increase of polarity of chemical bond ($\mu_{\text{N-B}} = 0.95 \text{ D}$) in support, for Pd₅/h-BN, a net electron transfer of only 0.029 |e| from the Pd cluster to support. Detailed inspection into bader charge shows that the charge located in B atoms increased by 0.166 |e| and the charge located in the adjacent N atom decreased by 0.137 |e|. This infers B and N atoms tend to localize and delocalize charge by receiving and releasing electrons to the Pd atoms, respectively, manifesting the process of “electron donation-back donation”. More interestingly, with the introduction of O—B bond with larger ionic ($\mu_{\text{O-B}} = 4.52 \text{ D}$), the increased polarity of support breaks the “electron donation-back donation” process and results in a reversal of charge transfer direction between Pd NPs and support, and thus inducing the electron transfer of 0.915 |e| from h-BNO to Pd NPs which form electron-rich Pd. This result demonstrates that the introduction of strong polar O—B bonds in the supports changed the electronic interactions between the Pd and supports, as well as the electronic structure of Pd NPs.

On one hand, compared to h-BN, a remarkable change in the electronic band structure for the h-BNO with strong polar O—B bond is that the Fermi level shifts upward into the conduction band, showing a typical n-type metallic character (in Fig. 6b). O—B impurity in h-BNO induces one occupied and one unoccupied defect state around the Fermi level (E_F) in the gap region, which are mainly composed of O p orbital

and B p orbital, acting as a donor and acceptor of electrons, respectively. It means that it is easier for O—B pair p-states to match with Pd d-states by donating and accepting electrons, thus enable electrons to transfer readily between them to form strong coupling O—B—Pd bonds. Furthermore, driven by the small energy difference between h-BNO highest occupied molecular orbital (HOMO) and Pd lowest unoccupied molecular orbital (LUMO) (in Fig. S15a,b) and the large work function mismatch (in Fig. S15c,d), electrons tend to transfer from h-BNO to Pd readily. After bonding with O—B, the Pd 4d states obtain electrons and move away from the Fermi level making the system stable.

On the other hand, as the electron accumulation on Pd, the d-band center (ϵ_d), serving as a descriptor of the catalytic performance for transition metal, will undergo downshift relative to the Fermi level in order to maintain the fixed d occupancy. Fig. 6c shows that ϵ_d of Pd₅/h-BN-O ($\epsilon_d = -2.01 \text{ eV}$) is very close to that of Pt₅/Graphene ($\epsilon_d = -2.17 \text{ eV}$) but is significantly lower than those of Pd(111) ($\epsilon_d = -1.43 \text{ eV}$) [47], Pd₅/Graphene ($\epsilon_d = -1.40 \text{ eV}$) and Pd₅/h-BN ($\epsilon_d = -1.45 \text{ eV}$), indicating that O—B bond modifies the electronic structure of Pd NPs so that it is similar to that of Pt NPs loaded on graphene.

The effects of O—B content on the ORR activity of Pd/BNO have been assessed and the results are shown in Fig. S14a. With the increase of O—B bonds, the number of electron transferred from BNO to Pd increased, which results in a further downshift of d-band center for Pd/h-BNO (Fig. S14b). However, as the O—B/N—B ratio increases from 4.2% to 19.0%, the number of electron transferred tends to a stable value, and accordingly, the d-band center of Pd is down-shifted to a constant value ($\epsilon_d = -2.01 \text{ eV}$), which is very close to that of Pt/Graphene ($\epsilon_d = -2.17 \text{ eV}$). The phenomena indicate that an excessive content of O—B bonds in h-BNO is nearly ineffective to further enhance the catalytic

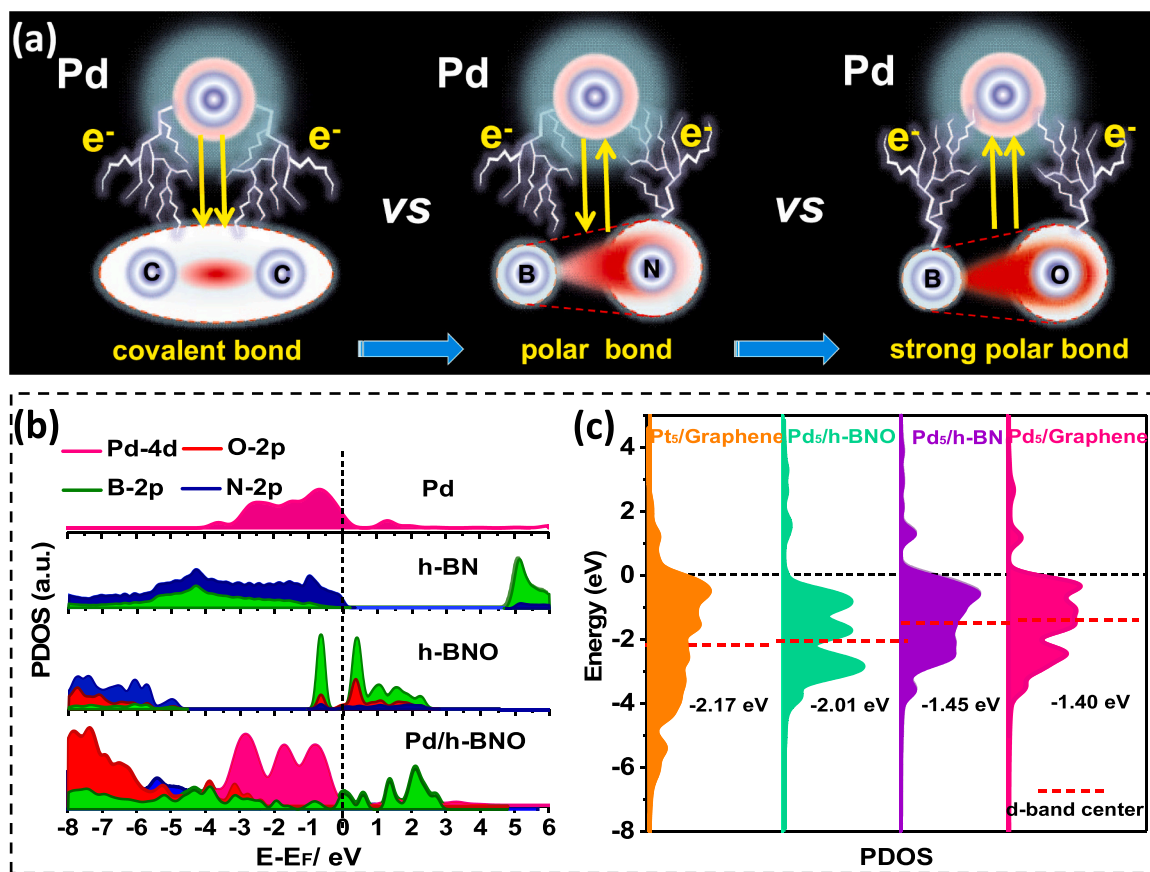


Fig. 6. (a) Design strategy to regulate the surface polarity of support and the direction of electron transfer between Pd and support, while gradually forming the electron-rich state of Pd catalyst. (b) The partial density of states (PDOS) of the d-state for Pd (with or without support) and the p-state for B, N and O from the h-BN and h-BNO (with or without Pd), respectively. (c) The d-band centers for Pd₅/Graphene, Pd₅/h-BN, Pd₅/h-BNO, and Pt₅/Graphene. The O—B/N—B ratio in h-BNO is 13.60%.

performance of Pd/h-BNO for ORR. It is noted that the theoretically simulated O–B content value and derived d-state values (by DFT) are underestimated compared with the experimental figures because of electron self-interaction error.

3.5.3. Evaluation of ORR catalytic performance

The electron transfer effect between h-BNO support and Pd was further analyzed, which has three important impacts on ORR:

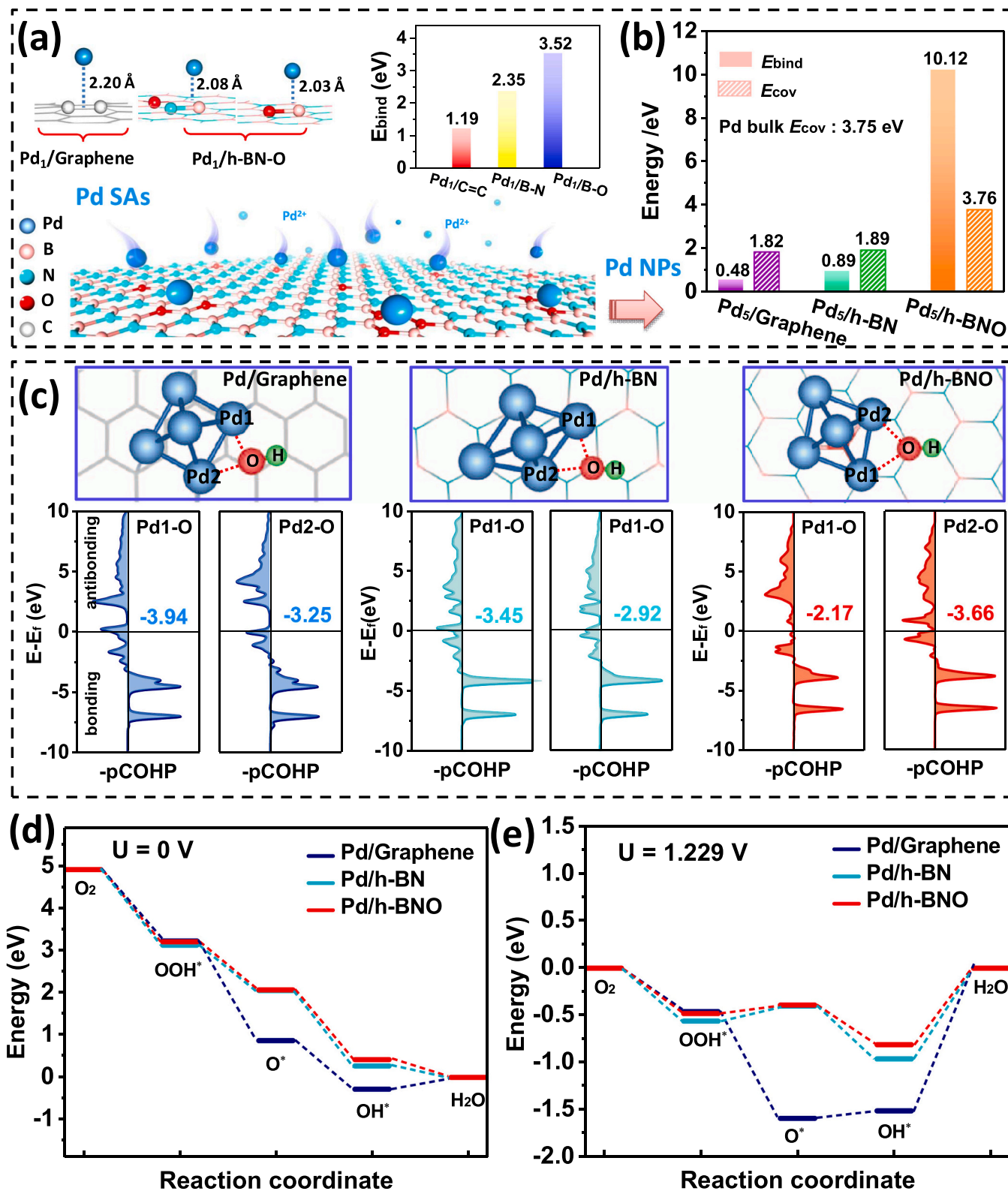


Fig. 7. (a, b) Mechanistic scheme of binding energy between Pd and support as a function of increasing SMSI effect, regulated by the polarity of the support. (c) Projected Crystal Orbital Hamilton population (pCOHP) between the catalysts and the adsorbed OH, and the corresponding ICOHP values. (d, e) The free energy diagrams of ORR on Pd₅/Graphene, Pd₅/h-BN and Pd₅/h-BNO at 0 V and 1.229 V (vs.NHE). The O–B/N–B ratio in h-BNO is 13.6%.

- (i) Enhancing the interaction between metal and support. The deposition selectivities of single Pd atoms (SAs) and durability of Pd cluster (regarded as NPs) on graphene and h-BNO sheets were checked. As shown in Fig. 7a, the Pd atom tends to bind on the bridge site of covalent C=C bond in graphene with the distance of 2.20 Å and binding energy (E_{bind}) of 1.19 eV. For h-BNO sheet containing both B—N and B—O bonds, Pd atom tends to locate on O—B bond and close to B with a shorter distance of 2.03 Å and a larger E_{bind} of 3.52 eV (for N—B bond, 2.08 Å and 2.35 eV), illustrating strong polar chemical bond in support improves the coupling between Pd and support. As shown in Fig. 7b, the E_{bind} between Pd₅ cluster and graphene, h-BN and h-BNO was calculated to be 0.48 eV, 0.89 eV and 10.20 eV, indicating that polar chemical bond in support can anchor Pd NPs more effectively. Actually, the E_{bind} values of both Pd₅/Graphene and Pd₅/h-BN are lower than the corresponding cohesive energy (E_{cov}), suggesting that Pd NPs on graphene and h-BN tend to aggregate [48, 49]. Surprisingly, the E_{bind} of Pd₅/h-BNO is much larger than the corresponding E_{cov} (3.76 eV) and bulk Pd E_{cov} (3.75 eV). This result is in good agreement with experimental results, revealing the excellent durability of Pd/p-BNO is originated from the strong interaction between Pd and O—B site with larger polarity.
- (ii) Optimizing the adsorption of oxygen intermediates. To investigate the Pd—O bond strength directly, the integrated Crystal Orbital Hamiltonian Population (ICOHP) for Pd—O bond was further performed on each model (Fig. 7c). The OH* (* denotes the adsorption state) intermediate was adsorbed above on Pd—Pd bond of catalysts and bonded with two Pd atoms, thereby two ICOHP values of Pd—OH bonds were calculated, where the more negative ICOHP values, the stronger binding strength between Pd and *OH [50,51]. As results are analyzed, the order of total ICOHP value for Pd—OH* on catalysts was Pd₅/h-BNO (−5.83) < Pd₅/h-BN (−6.37) < Pd₅/Graphene (−7.19). In contrast, the excessive bonding interaction between OH* and Pd/Graphene and Pd/h-BN catalysts can bring about insurmountable OH* desorption or hampered conversion of *OH to H₂O, and therefore resulting in poor ORR activity. However, the enhanced ICOHP value on Pd₅/h-BNO means an enlarged gap between the Pd d orbital and the p orbital of oxygenated intermediates, thus alleviates the over-binding of oxygenated intermediates on the Pd catalysts surface (Table S3), facilitating ORR process.
- (iii) Lowering the Gibbs free energy of ORR process. The free energy diagrams were calculated to illustrate ORR pathways on Pd₅/Graphene, Pd₅/h-BN and Pd₅/h-BNO catalysts at 0 V and 1.229 V (vs.NHE), respectively (Section S2, Table S4). As shown in Fig. 7d, due to the strong strength between Pd based catalysts and OH* intermediate, the rate-determining step (RDS) of ORR was the formation of H₂O product (OH* + e[−] + H⁺ → H₂O). While for Pd₅/h-BN and Pd₅/h-BNO, as a result of the weak binding strength, the RDSs show entirely smooth downhill routes, revealing excellent reactivity to the acidic ORR. Correspondingly, when U = 1.229 V vs.NHE (Fig. 7e), the formation of reaction product H₂O became easier from Pd/Graphene to Pd₅/h-BNO with a lower free energy change of the last step. The ΔG_{max} value was decreased from 1.51 eV (for Pd₅/Graphene) to 0.96 eV (for Pd₅/h-BN) and then to 0.81 eV (for Pd₅/h-BNO), thus facilitating the overall ORR process. Overall, excellent ORR performance of Pd₅/h-BNO was originated from the directed transfer of electrons from h-BNO to Pd atoms, which driving by strong polar bonds on support.

4. Conclusion

In summary, we reported strong metal-support interaction strategy induced by strong polar bonds on the support surface to tailor the electronic structure and surface charge of Pd and hence results in both

high activity and excellent durability for ORR. In alkaline media, the optimized catalyst Pd/p-BNO-2 exhibits 0.253 A mg^{−1}_{Pd} and 0.413 mA cm^{−2} in MA and SA respectively, which are 4.1 and 2.9 times those of Com. Pd/C, and even 1.9 and 2.2-fold higher than those of Com. Pt/C. Furthermore, the Pd/p-BNO exhibits substantially better stability than both Com. Pd/C and Pt/C, with almost no degradation in ORR activity observed during 5000 cycles of ADT test in both alkaline and acidic media. The excellent ORR performance of Pd/p-BNO was ascribed to the following reasons: first, the polar bonds in support provide effective anchoring sites for the formation and subsequent attachment of Pd NPs. Second, the polar bonds in support enable the electron directional transfer from support to Pd NPs, which lead to an electron-rich Pd surface and a down-shift of d band center. Third, the electron-rich Pd surface played a crucial role in improving oxygen reduction activity by optimizing the adsorption of oxygenated intermediate species and reducing the ORR free energy. This work provides a fundamental understanding of the vital roles of polar bonds in the supports on boosting the catalytic activity of metal in the newly developed system and encourage more effort along this interesting direction.

CRedit authorship contribution statement

Lanlan Li and **Qiaoling Li**: Conceived ideas, designed experiments and co-wrote the paper. **Qiaoling Li**, **Xiaoqing Yang** and **Zhi Xie**: Synthesized samples and studied their structure and electrochemical properties. **Qiaoling Li**, **Xuwei Wang**, **Xiaofei Yu**, and **Lingli Guo**: Conducted the density functional theory calculations. **Xingkai Peng** and **Xinghua Zhang**: Helped with the synthesis of materials. **Lanlan Li** and **Zunming Lu**: Helped with the electrocatalytic tests and data analyses.

Declaration of Competing Interest

The authors declare that they have no known competing financial interests or personal relationships that could have appeared to influence the work reported in this paper.

Acknowledgements

This work was supported by the National Natural Science Foundation of China (Grant No. 22179032, 51771068, 51771067, 51871088), and the Natural Science Foundation of Hebei Province (Grant No. B2021202011, E2021202022, B2019202194, E2019202048).

Appendix A. Supporting information

Supplementary data associated with this article can be found in the online version at doi:10.1016/j.apcatb.2021.121020.

References

- [1] E. Antolini, Palladium in fuel cell catalysis, *Energy Environ. Sci.* 2 (2009) 915–931, <https://doi.org/10.1039/b820837a>.
- [2] S. Buchele, Z. Chen, E. Fako, F. Krumeich, R. Hauert, O.V. Safonova, N. Lopez, S. Mitchell, J. Perez-Ramirez, Carrier-induced modification of palladium nanoparticles on porous porous nitride for alkyne semi-hydrogenation, *Angew. Chem. Int. Ed.* 59 (2020) 19639–19644, <https://doi.org/10.1002/anie.202005842>.
- [3] J.K. Nørskov, J. Rossmeisl, A. Logadottir, L. Lindqvist, J.R. Kitchin, T. Bligaard, J. Hanne, Origin of the overpotential for oxygen reduction at a fuel-cell cathode, *J. Phys. Chem. B* 108 (2004) 17886–17892, <https://doi.org/10.1021/jp047349j>.
- [4] Y. Nie, L. Li, Z.D. Wei, Recent advancements in Pt and Pt-free catalysts for oxygen reduction reaction, *Chem. Soc. Rev.* 44 (2015) 2168–2201, <https://doi.org/10.1039/c4cs00484a>.
- [5] M.K. Debe, Electrocatalyst approaches and challenges for automotive fuel cells, *Nature* 486 (2012) 43–51, <https://doi.org/10.1038/nature11115>.
- [6] M. Zhou, J. Guo, B. Zhao, C. Li, L. Zhang, J. Fang, Improvement of oxygen reduction performance in alkaline media by tuning phase structure of Pd-Bi nanocatalysts, *J. Am. Chem. Soc.* 143 (2021) 15891–15897, <https://doi.org/10.1021/jacs.1c08644>.
- [7] J. Li, J.X. Chen, Q. Wang, W.B. Cai, S.L. Chen, Controllable increase of boron content in B-Pd interstitial nanoalloy to boost the oxygen reduction activity of

- palladium, *Chem. Mater.* 29 (2017) 10060–10067, <https://doi.org/10.1021/acs.chemmater.7b03732>.
- [8] J.X. Fan, H.X. Du, Y. Zhao, Q. Wang, Y.N. Liu, D.Q. Li, J.T. Feng, Recent progress on rational design of bimetallic Pd based catalysts and their advanced catalysis, *ACS Catal.* 10 (2020) 13560–13583, <https://doi.org/10.1021/acscatal.0c03280>.
 - [9] T.W. van Deelen, C.H. Mejía, K.P. de Jong, Control of metal-support interactions in heterogeneous catalysts to enhance activity and selectivity, *Nat. Catal.* 2 (2019) 955–970, <https://doi.org/10.1038/s41929-019-0364-x>.
 - [10] Q. Xue, J. Bai, C.C. Han, P. Chen, J.X. Jiang, Y. Chen, Au nanowires@Pd-polyethylenimine nanohybrids as highly active and methanol-tolerant electrocatalysts toward oxygen reduction reaction in alkaline media, *ACS Catal.* 8 (2018) 11287–11295, <https://doi.org/10.1021/acscatal.8b03447>.
 - [11] L. Zhao, R. Wu, J. Wang, Z. Li, X. Wei, J.S. Chen, Y. Chen, Synthesis of noble metal-based intermetallic electrocatalysts by space-confined pyrolysis: recent progress and future perspective, *J. Energy Chem.* 60 (2021) 61–74, <https://doi.org/10.1016/j.jechem.2020.12.021>.
 - [12] Y. Zhao, L.J. Yang, S. Chen, X.Z. Wang, Y.W. Ma, Q. Wu, Y.F. Jiang, W.J. Qian, Z. Hu, Can boron and nitrogen co-doping improve oxygen reduction reaction activity of carbon nanotubes? *J. Am. Chem. Soc.* 135 (2013) 1201–1204, <https://doi.org/10.1021/ja310566z>.
 - [13] J.T. Grant, C.A. Carrero, F. Goeltl, J. Venegas, P. Mueller, S.P. Burt, S.E. Specht, W. P. McDermott, A. Chiericato, I. Hermans, Selective oxidative dehydrogenation of propane to propene using boron nitride catalysts, *Science* 354 (2016) 1570–1573, <https://doi.org/10.1126/science.1257885>.
 - [14] X.W. Zhong, S.L. Ye, J. Tang, Y.M. Zhu, D.J. Wu, M. Gu, H. Pan, B.M. Xu, Engineering Pt and Fe dual-metal single atoms anchored on nitrogen-doped carbon with high activity and durability towards oxygen reduction reaction for zinc-air battery, *Appl. Catal. B* 286 (2021), 119891, <https://doi.org/10.1016/j.apcatb.2021.119891>.
 - [15] Y.Y. Meng, D. Voiry, A. Goswami, X.X. Zou, X.X. Huang, M. Chhowalla, Z.W. Liu, T. Asefa, N., O., and S-tridoped nanoporous carbons as selective catalysts for oxygen reduction and alcohol oxidation reactions, *J. Am. Chem. Soc.* 136 (2014) 13554–13557, <https://doi.org/10.1021/ja507463w>.
 - [16] L.J. Yang, S.J. Jiang, Y. Zhao, L. Zhu, S. Chen, X.Z. Wang, Q. Wu, J. Ma, Y. Ma, Z. Hu, Boron-doped carbon nanotubes as metal-free electrocatalysts for the oxygen reduction reaction, *Angew. Chem. Int. Ed.* 50 (2011) 7132–7135, <https://doi.org/10.1002/anie.201101287>.
 - [17] Z.H. Zhao, Z.H. Xia, Design principles for dual-element-doped carbon nanomaterials as efficient bifunctional catalysts for oxygen reduction and evolution reactions, *ACS Catal.* 6 (2016) 1553–1558, <https://doi.org/10.1021/acscatal.5b02731>.
 - [18] X.F. Zhu, C.G. Hu, R. Amal, L.M. Dai, X.Y. Lu, Heteroatom-doped carbon catalysts for zinc-air batteries: progress, mechanism, and opportunities, *Energy Environ. Sci.* 13 (2020) 4536–4563, <https://doi.org/10.1039/d0ee02800b>.
 - [19] C.Z. Zhang, N. Mahmood, H. Yin, F. Liu, Y.L. Hou, Synthesis of phosphorus-doped graphene and its multifunctional applications for oxygen reduction reaction and lithium ion batteries, *Adv. Mater.* 25 (2013) 4932–4937, <https://doi.org/10.1002/adma.201301870>.
 - [20] Q.W. Chang, P. Zhang, A.H.B. Mostaghimi, X.R. Zhao, S.R. Denny, J.H. Lee, H. P. Gao, Y. Zhang, H.L.L. Xin, S. Siahrostami, J.G.G. Chen, Z. Chen, Promoting H₂O₂ production via 2-electron oxygen reduction by coordinating partially oxidized Pd with defect carbon, *Nat. Commun.* 11 (2020) 2178, <https://doi.org/10.1038/s41467-020-15843-3>.
 - [21] C. Zhang, S.S. Yu, Y.N. Xie, W. Zhang, K. Zheng, N.E. Drewett, S.J. Yoo, Z.Z. Wang, L.D. Shao, H.W. Tian, J.G. Kim, W.T. Zheng, Suppressing the Pd-C interaction through B-doping for highly efficient oxygen reduction, *Carbon* 149 (2019) 370–379, <https://doi.org/10.1016/j.carbon.2019.04.060>.
 - [22] S. Kabir, A. Serov, K. Artyushkova, P. Atanassov, Nitrogen-doped three-dimensional graphene-supported palladium nanocomposites: high-performance cathode catalysts for oxygen reduction reactions, *ACS Catal.* 7 (2017) 6609–6618, <https://doi.org/10.1021/acscatal.7b02071>.
 - [23] R. Arrigo, M.E. Schuster, Z.L. Xie, Y.M. Yi, G. Wowsnick, L.L. Sun, K.E. Hermann, M. Friedrich, P. Kast, M. Hävecker, A. Knop-Gericke, R. Schlögl, Nature of the N-Pd interaction in nitrogen-doped carbon nanotube catalysts, *ACS Catal.* 5 (2015) 2740–2753, <https://doi.org/10.1021/acscatal.5b00094>.
 - [24] J. Pu, K. Zhang, Z.H. Wang, C.W. Li, K.P. Zhu, Y.G. Yao, G. Hong, Synthesis and modification of boron nitride nanomaterials for electrochemical energy storage: from theory to application, *Adv. Funct. Mater.* 31 (2021), 2106315, <https://doi.org/10.1002/adfm.202106315>.
 - [25] M. Weber, N. Tuleushova, J. Zgheib, C. Lamboux, I. Iatsunskyi, E. Coy, V. Flaud, S. Tingry, D. Cornu, P. Miele, M. Bechelany, Y. Holade, Enhanced electrocatalytic performance triggered by atomically bridged boron nitride between palladium nanoparticles and carbon fibers in gas-diffusion electrodes, *Appl. Catal. B* 257 (2019), 117917, <https://doi.org/10.1016/j.apcatb.2019.117917>.
 - [26] H. Liu, X.H. Zhang, Y.X. Li, X. Li, C.K. Dong, D.Y. Wu, C.C. Tang, S.L. Chou, F. Fang, X.W. Du, Conductive boron nitride as promising catalyst support for the oxygen evolution reaction, *Adv. Energy Mater.* 10 (2020), 1902521, <https://doi.org/10.1002/aenm.201902521>.
 - [27] S.B. Tang, Q. Dang, T.Y. Liu, S.Y. Zhang, Z.G. Zhou, X.K. Li, X.J. Wang, E. Sharman, Y. Luo, J. Jiang, Realizing a not-strong-not-weak polarization electric field in single-atom catalysts sandwiched by boron nitride and graphene sheets for efficient nitrogen fixation, *J. Am. Chem. Soc.* 142 (2020) 19308–19315, <https://doi.org/10.1021/jacs.0c09527>.
 - [28] S. Zhou, X.W. Yang, X. Xu, S.X. Dou, Y. Du, J.J. Zhao, Boron nitride nanotubes for ammonia synthesis: activation by filling transition metals, *J. Am. Chem. Soc.* 142 (2020) 308–317, <https://doi.org/10.1021/jacs.9b10588>.
 - [29] M.M. Sun, J.C. Dong, Y. Lv, S.Q. Zhao, C.X. Meng, Y.J. Song, G.X. Wang, J.F. Li, Q. Fu, Z.Q. Tian, X.H. Bao, Pt@h-BN core-shell fuel cell electrocatalysts with electrocatalysis confined under outer shells, *Nano Res.* 11 (2018) 3490–3498, <https://doi.org/10.1007/s12274-018-2029-5>.
 - [30] Y.P. Chen, J.Y. Cai, P. Li, G.Q. Zhao, G.M. Wang, Y.Z. Jiang, J. Chen, S.X. Dou, H. G. Pan, W.P. Sun, Hexagonal boron nitride as a multifunctional support for engineering efficient electrocatalysts toward the oxygen reduction reaction, *Nano Lett.* 20 (2020) 6807–6814, <https://doi.org/10.1021/acs.nanolett.0c02782>.
 - [31] Q.L. Li, L.L. Li, X.F. Yu, X.Y. Wu, Z. Xie, X.W. Wang, Z.M. Lu, X.H. Zhang, Y. Huang, X.J. Yang, Ultrafine platinum particles anchored on porous boron nitride enabling excellent stability and activity for oxygen reduction reaction, *Chem. Eng. J.* 399 (2020), 125827, <https://doi.org/10.1016/j.cej.2020.125827>.
 - [32] C.Z. Wu, B. Wang, N. Wu, C. Han, X.S. Zhang, S.J. Shen, Q. Tian, C. Qin, P.P. Li, Y. D. Wang, Molecular-scale understanding on the structure evolution from melamine diborate supramolecule to boron nitride fibers, *Ceram. Int.* 46 (2020) 1083–1090, <https://doi.org/10.1016/j.ceramint.2019.09.075>.
 - [33] D.D. Koelling, B.N. Harmon, A technique for relativistic spin-polarised calculations, *J. Phys. C Solid State Phys.* 10 (1977) 3107–3114, <https://doi.org/10.1088/0022-3719/10/16/019>.
 - [34] G. Kresse, J. Furthmüller, Efficiency of ab-initio total energy calculations for metals and semiconductors using a plane-wave basis set, *Comp. Mater. Sci.* 6 (1996) 15–50, [https://doi.org/10.1016/0927-0256\(96\)00008-0](https://doi.org/10.1016/0927-0256(96)00008-0).
 - [35] J.P. Perdew, K. Burke, M. Ernzerhof, Generalized gradient approximation made simple, *Phys. Rev. Lett.* 77 (1998) 3865–3868, <https://doi.org/10.1103/physrevlett.77.3865>.
 - [36] Q.H. Weng, D.G. Kvashnin, X. Wang, O. Cretu, Y. Yang, M. Zhou, C. Zhang, D. M. Tang, P.B. Sorokin, Y. Bando, D. Golberg, Tuning of the optical, electronic, and magnetic properties of boron nitride nanosheets with oxygen doping and functionalization, *Adv. Mater.* 29 (2017), 1700695, <https://doi.org/10.1002/adma.201700695>.
 - [37] Y.H. Cao, R.Y. Zhang, T.L. Zhou, S.M. Jin, J.D. Huang, L.Q. Ye, Z.A. Huang, F. Wang, Y. Zhou, B-O bonds in ultrathin boron nitride nanosheets to promote photocatalytic carbon dioxide conversion, *ACS Appl. Mater. Interfaces* 12 (2020) 9935–9943, <https://doi.org/10.1021/acsaami.9b21157>.
 - [38] Q.H. Weng, X.B. Wang, C.Y. Zhi, Y. Bando, D. Golberg, Boron nitride porous microbelts for hydrogen storage, *ACS Nano* 7 (2013) 1558–1565, <https://doi.org/10.1021/nn305320v>.
 - [39] G. Postole, M. Caldararu, B. Bonnetot, A. Auroux, Influence of the support surface chemistry on the catalytic performances of PdO/BN catalysts, *J. Phys. Chem. C* 112 (2008) 11385–11393, <https://doi.org/10.1021/jp803963e>.
 - [40] C.Y. Zhi, Y. Bando, C.C. Tang, D. Golberg, R.G. Xie, T. Sekigushi, Phonon characteristics and cathodoluminescence of boron nitride nanotubes, *Appl. Phys. Lett.* 86 (2005), 213110, <https://doi.org/10.1063/1.1938002>.
 - [41] C.C. Tang, Y. Bando, Y. Huang, C.Y. Zhi, D. Golberg, Synthetic routes and formation mechanisms of spherical boron nitride nanoparticles, *Adv. Funct. Mater.* 18 (2008) 3653–3661, <https://doi.org/10.1002/adfm.200800493>.
 - [42] W. Zhou, P. Xiao, Y. Li, L. Zhou, Dielectric properties of BN modified carbon fibers by dip-coating, *Ceram. Int.* 39 (2013) 6569–6576, <https://doi.org/10.1016/j.ceramint.2013.01.090>.
 - [43] C.J. Huang, C. Chen, M.W. Zhang, L.H. Lin, X.X. Ye, S. Lin, M. Antonietti, X. C. Wang, Carbon-doped BN nanosheets for metal-free photoredox catalysis, *Nat. Commun.* 6 (2015) 698, <https://doi.org/10.1038/ncomms8698>.
 - [44] Y. Lu, J. Wang, Y. Peng, A. Fisher, X. Wang, Highly efficient and durable Pd hydride nanocubes embedded in 2D amorphous NiB nanosheets for oxygen reduction reaction, *Adv. Energy Mater.* 7 (2017), 1700919, <https://doi.org/10.1002/aenm.201700919>.
 - [45] L. Gao, M.C. Zhu, Z.Y. Zhang, G.L. Cui, Cobalt-boron-oxide supported on N, P dual-doped carbon nanosheets as the trifunctional electrocatalyst and its application in rechargeable Zn-air battery and overall water-electrolysis, *Electrochim. Acta* 327 (2019), 134980, <https://doi.org/10.1016/j.electacta.2019.134980>.
 - [46] J. Zhang, Z.Y. Wang, W.X. Chen, Y. Xiong, W.C. Cheong, L.R. Zheng, W.S. Yan, L. Gu, C. Chen, Q. Peng, P. Hu, D.S. Wang, Y.D. Li, Tuning polarity of Cu-O bond in heterogeneous Cu catalyst to promote additive-free hydroboration of alkynes, *Chem* 6 (2020) 725–737, <https://doi.org/10.1016/j.chempr.2019.12.021>.
 - [47] J.C. Guo, L. Gao, X. Tan, Y.L. Yuan, J. Kim, Y. Wang, H. Wang, Y.J. Zeng, S. Choi, S. C. Smith, H.W. Huang, Template-directed rapid synthesis of Pd-based ultrathin porous intermetallic nanosheets for efficient oxygen reduction, *Angew. Chem. Int. Ed.* 60 (2021) 10942–10949, <https://doi.org/10.1002/anie.202100307>.
 - [48] C.F. Deng, R.X. He, W. Shen, M. Li, Theoretical analysis of oxygen reduction reaction activity on single metal (Ni, Pd, Pt, Cu, Ag, Au) atom supported on defective two-dimensional boron nitride materials, *Phys. Chem. Chem. Phys.* 21 (2019) 18589–18594, <https://doi.org/10.1039/c9cp03287h>.
 - [49] C.F. Deng, R.X. He, D.M. Wen, W. Shen, M. Li, Theoretical study on the origin of activity for oxygen reduction reaction of metal doped two-dimensional boron nitride materials, *Phys. Chem. Chem. Phys.* 20 (2018) 10240–10246, <https://doi.org/10.1039/c8cp00838h>.
 - [50] M.A. Hunter, J.M.T.A. Fischer, Q. Yuan, M. Hankel, D.J. Searles, Evaluating the catalytic efficiency of paired, single-atom catalysts for the oxygen reduction reaction, *ACS Catal.* 9 (2019) 7660–7667, <https://doi.org/10.1021/acscatal.9b02178>.
 - [51] N.Q. Zhang, X.X. Zhang, Y.K. Kang, C.L. Ye, R. Jin, H. Yan, R. Lin, J.R. Yang, Q. Xu, Y. Wang, Q.H. Zhang, L. Gu, L.C. Liu, W.Y. Song, J. Liu, D.S. Wang, Y.D. Li, A supported Pd₂ dual-atom site catalyst for efficient electrochemical CO₂ reduction, *Angew. Chem. Int. Ed.* 60 (2021) 13388–13393, <https://doi.org/10.1002/anie.202101559>.